Chemical Science

ROYAL SOCIETY OF CHEMISTRY

EDGE ARTICLE

View Article Online
View Journal | View Issue



Cite this: *Chem. Sci.*, 2024, **15**, 4106

All publication charges for this article have been paid for by the Royal Society of Chemistry

# Polar alcohol guest molecules regulate the stacking modes of 2-D MOF nanosheets†

Yue Cheng, ‡ Wen-Qi Tang,‡ Lu-Ting Geng, Ming Xu, Jian-Ping Zhu, Sha-Sha Meng and Zhi-Yuan Gu *

Received 20th December 2023
Accepted 7th February 2024

DOI: 10.1039/d3sc06844g

rsc.li/chemical-science

The modulation of two-dimensional metal–organic framework (2-D MOF) nanosheet stacking is an effective means to improve the properties and promote the application of nanosheets in various fields. Here, we employed a series of alcohol guest molecules (MeOH, EtOH and PrOH) to modulate Zr–BTB (BTB = benzene-1,3,5-tribenzoate) nanosheets and to generate untwisted stacking. The distribution of stacking angles was statistically analyzed from high-angle annular dark-field (HAADF) and fast Fourier transform (FFT) images. The ratios of untwisted stacking were calculated, such as 77.01% untwisted stacking for MeOH, 83.45% for EtOH, and 85.61% for PrOH. The obtained untwisted Zr–BTB showed good separation abilities for different substituted benzene isomers, superior *para* selectivity and excellent column stability and reusability. Control experiments of 2-D Zr–TCA (TCA = 4,4′,4″-tricarboxytriphenylamine) and Zr–TATB (TATB = 4,4′,4″-(1,3,5-triazine-2,4,6-triyl)tribenzoic acid) nanosheets with similar pore sizes and stronger polarity regulated by the alcohol guests exhibited moderate separation performance. The electron microscopy images revealed that polar alcohol regulation dominantly generated the twisted stacking of Zr–TCA and Zr–TATB with various Moiré patterns. Polar guest molecules, such as alcohols, provide strong host–guest interactions during the regulation of MOF nanosheet stacking, providing an opportunity to design new porous Moiré materials with application prospects.

## Introduction

Twistronics is an emerging research area to study the twist between two layers of two-dimensional (2-D) materials.[1–4] The twist angle between adjacent layers of 2-D materials, such as graphene, $MoS_2$ and $WS_2$, provides a peculiar degree of freedom to generate Moiré patterns and to create novel properties including a highly adjustable band gap and extraordinary carrier transport properties.[5–7] For instance, Cao achieved the transformation from a graphene insulator to a superconductor by twisting double-layer graphene at an angle of ~1.1°.[8] Lin, by adjusting the torsion angle, altered the Raman modes of Moiré phonons between adjacent $MoS_2$.[9] Xie utilized twisted $WS_2$ as a hydrogen production catalyst, enhancing the activity of electrocatalysis.[10] Thus, manipulating the stacking modes between layers of 2-D materials can effectively tune the properties of these emerging layered materials.

2-D metal–organic frameworks (MOFs) are a new class of porous materials constructed from inorganic metal ions/clusters and organic ligands, and are ultrathin in the third dimension.[11–17] Compared to traditional porous materials, the superior structural features of 2-D MOFs, such as high surface area, high porosity, high stability, adjustable pore size, and functionalized pore surface, make them beneficial for the separation of important chemical raw materials, such as xylene isomers.[18–23] However, 2-D MOF nanosheets are too thin and easy to stack at random, which will block the pores that originally adsorb and separate gases, resulting in a reduced gas adsorption rate and separation efficiency.[24–26] Therefore, it is exceedingly essential and important to regulate the stacking modes of 2-D MOF nanosheets to improve the effect of gas adsorption and separation, which was largely neglected before.

Very few studies attempted the regulation approaches and discovered heating and host–guest noncovalent interactions were crucial to regulate the twisted and untwisted stacking modes.[27–29] Tao used the heating method to generate Zr–O–Zr bonds between the adjacent MOF layers to form the untwisted stacking. Then, a series of solvent molecules, such as nonpolar alkanes and weak polar methylbenzene were employed to regulate the stacking of the nanosheets. The hydrophobic nonpolar alkanes (dipole moment around 0 D) were found to induce 2-D MOF nanosheets into a regular packing mode, while medium polar methylbenzene (dipole moment is 0.4 D) induced the nanosheets to the twisted stacking mode. However, the molecules with strong polarity have not been studied yet.

*Jiangsu Key Laboratory of Biofunctional Materials, Jiangsu Collaborative Innovation Center of Biomedical Functional Materials, Jiangsu Key Laboratory of New Power Batteries, School of Chemistry and Materials Science, Nanjing Normal University, Nanjing, 210023, China. E-mail: guzhiyuan@njnu.edu.cn*

† Electronic supplementary information (ESI) available. See DOI: https://doi.org/10.1039/d3sc06844g

‡ Yue Cheng and Wen-Qi Tang contributed equally.

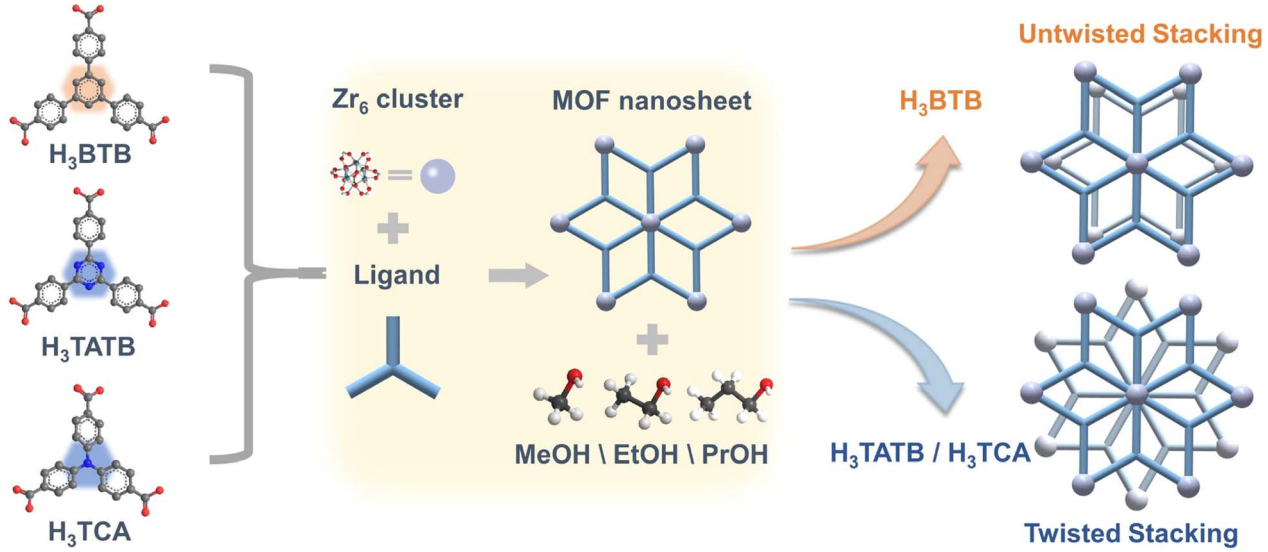


Scheme 1 The schematic diagram of modulating the stacking modes of 2-D MOF nanosheets through polar alcohol guest molecules.

Here, we proposed a new regulation method with polar alcohols, such as MeOH, EtOH and PrOH (dipole moments were 1.70 D, 1.66 D and 1.55 D, respectively) to regulate the stacking mode of 2-D MOF nanosheets (Scheme 1).[30] The zirconium-based MOF, Zr–BTB (BTB = benzene-1,3,5-tribenzoate) nanosheet, was selected as a model due to the ultrathin thickness and high stability.

The regulated materials were characterized by scanning electron microscopy (SEM), transmission electron microscopy (TEM) and atomic force microscopy (AFM), revealing the structure of stacked nanosheets. Further high-angle annular dark-field (HAADF) and fast Fourier transform (FFT) images counterintuitively showed untwisted stacking. The proportion of 0 degrees was as high as 77.01%, 83.45% and 85.61% for Zr–BTB–MeOH, Zr–BTB–EtOH and Zr–BTB–PrOH, respectively. These untwisted 2-D Zr–BTB capillary columns exhibited good separation ability. The isostructural 2-D Zr–TCA (TCA = 4,4′,4″-tricarboxytriphenylamine) and Zr–TATB (TATB = 4,4′,4″-(1,3,5-triazine-2,4,6-triyl)tribenzoic acid) nanosheets with much higher polarity were also modulated by polar alcohol as a comparison. However, the 2-D Zr–TCA–MeOH was dominantly twisted stacking with rotation angles of 6°, 12°, 18°, 24° and 30°, and Zr–TATB–EtOH with angles of 0°, 6°, 10°, 12° 15°, 18°, and 24°, which led to poor separation performance.

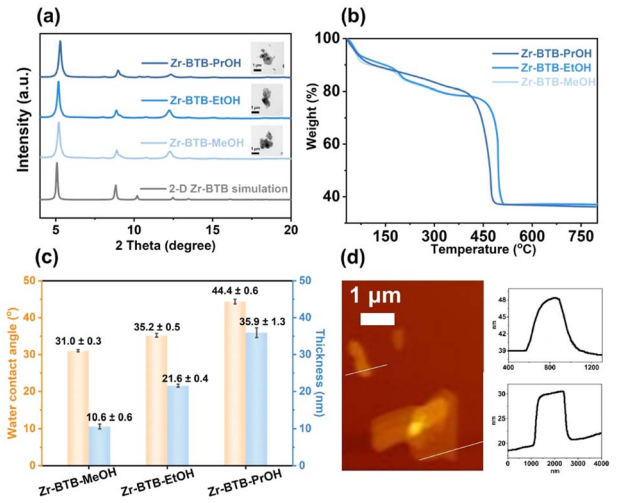


Fig. 1 The characterization of 2-D Zr–BTB. (a) PXRD patterns and TEM images of Zr–BTB–MeOH, Zr–BTB–EtOH, Zr–BTB–PrOH and simulated 2-D Zr–BTB; (b) TGA curves; (c) water contact angle and thickness; (d) AFM image of Zr–BTB–MeOH.

## Results and discussion

### Synthesis and characterization of stacked 2-D Zr–BTB nanosheets induced by polar alcohols

In the 2-D Zr–BTB nanosheets, the $Zr_6$ cluster acts as metallic nodes that are occupied by six $H_3BTB$ linkers in the planar fashion, where the remaining six edges of the $Zr_6$ cluster are connected by acid modulators and water as capping reagents. HNMR indicated that $n(Zr_6\ clusters) : n(H_3BTB) : n(nanopore) : n(formic\ acid, FA) = 1 : 2 : 3 : 2$ (Fig. S2–S4†), showing that there were two FA modulators and four $H_2O/OH$ on each $Zr_6$ cluster. Although the aromatic BTB ligand showed weak polarity, the four $H_2O/OH$ sites on the $Zr_6$ cluster offered significant polarity. To explore alcohols as the regulation reagent, strongly polar MeOH, EtOH and PrOH solvents were selected to induce the stacking between the Zr–BTB nanosheets.

The Zr–BTB nanosheets were synthesized as reported.[31] The as-synthesized MOF nanosheets were washed with MeOH, EtOH and PrOH, respectively. For example, the Zr–BTB nanosheet was washed with 25 mL of MeOH for 5 minutes. After washing three times, the material was dried at 25 °C to eliminate MeOH. The sample was named Zr–BTB–MeOH. Other nanosheets were synthesized in a similar way and specific details of synthesis and washing steps are shown in the ESI.†

As seen in the PXRD patterns (Fig. 1a), the first two main peaks of the 2-D Zr–BTB nanosheets were attributed to the (011) and (002) planes, respectively, consistent with that of 2-D Zr–BTB simulation. It is proved that the crystalline structure of the three 2-D Zr–BTB nanosheets was successfully obtained after alcohol treatment. TGA of the 2-D Zr–BTB nanosheets was conducted in an oxygen atmosphere (Fig. 1b and S1†). First of all, it showed slight weight loss of the three MOFs in the range of 30–180 °C due to the loss of solvent molecules and free modulator molecules. And then it showed no significant weight loss at 180–405 °C. Finally, all MOFs decomposed gradually at >∼400 °C, forming the metal oxide phases of $ZrO_2$. The results also revealed the good thermal stability of the obtained 2-D MOF nanosheets.

To characterize the polarity differences of nanosheets, water contact angle experiments and HNMR experiments were performed. All the water contact angle measurements were carried out in the air at room temperature (Fig. 1c and S5–S7†). The increment of water contact angle was observed among Zr–BTB–MeOH (31.0 ± 0.3°), Zr–BTB–EtOH (35.2 ± 0.5°) and Zr–BTB–PrOH (44.4 ± 0.6°), indicating that more hydrophobicity came from the increasing alkyl chains. Due to the existence of the polar $H_2O$/OH sites on $Zr_6$ clusters as well as the alcohol hydroxyl group, the water contact angle of the nanosheets was much less than 90°, which reflected the highly hydrophilic property and strong polarity. At the same time, the number of polar $H_2O$/OH sites was unchanged during alcohol washing, which was confirmed by HNMR (Fig. S2–S4†). Furthermore, the specific ratios of alcohol molecule to $Zr_6$ cluster, such as $n(\text{MeOH}) : n(Zr_6)$ of 0.4, $n(\text{EtOH}) : n(Zr_6)$ of 0.3, and $n(\text{PrOH}) : n(Zr_6)$ of 1.0 were obtained (Fig. S2–S4†). The high ratios of methanol and ethanol to Zr clusters indicated the existence of significant amounts of methanol and ethanol, respectively, even after the drying procedure although they had high volatility. This proved that –OH and the polar $H_2O$/OH sites on $Zr_6$ clusters had strong polarity interaction. The higher amount of propanol residue was due to the higher boiling point and strong polarity interaction between –OH of PrOH and the $H_2O$/OH sites on $Zr_6$ clusters.

To characterize the morphology, the stacked nanosheets were measured by SEM and TEM (Fig. S8 and S9†). The SEM images of the three nanosheets showed many 2-D lamellar structures. The TEM images of Zr–BTB nanosheets revealed that the material was stacked with multilayers. According to TEM and SEM images, the size of nanosheets reached the micrometer level. In order to measure the thickness of the 2-D lamellar MOF, 2-D Zr–BTB nanosheets were characterized by AFM. The substrate of mica was flat, confirmed by blank measurements (Fig. S10†). To verify the influence of solvent, MeOH, EtOH, and PrOH was dropped on clean and smooth mica slices, respectively. It was found that the surface of the mica slices was basically smooth, and no obvious nanosheets appeared (Fig. S10†). Hence, MeOH, EtOH, and PrOH as solvent and mica as substrates were suitable for the characterization of nanosheets. The dispersion solvent of the nanosheet was the same as that of the washing solvent. According to AFM measurements (Fig. 1c and S11–S13†), the thicknesses of the Zr–BTB–MeOH, Zr–BTB–EtOH and Zr–BTB–PrOH nanosheets were 10.6 ± 0.6 nm, 21.6 ± 0.4 nm and 35.9 ± 1.3 nm, respectively. With the increasing alkyl chains, the thickness increased gradually because the interaction induced by the polar solvent was stronger.

## HAADF characterization and simulation of 2-D Zr–BTB nanosheets

To further explore the stacking modes of the three 2-D Zr–BTB nanosheets induced by polar molecules, HAADF images and FFT images were measured (Fig. 2). In the HAADF pictures, a white dot represented a $Zr_6$ cluster. Regular aligned $Zr_6$ clusters were obtained in most measurement areas of samples (Fig. 2a) and a characteristic FFT image was correspondingly obtained, which was in good agreement with the simulated 2-D nanosheet.

At the same time, the $Zr_6$ clusters of the nanosheet were misaligned between adjacent layers in other measurement areas, resulting in the emergence of a set of Moiré stripes. Then, the $Zr_6$ clusters were simplified into points and two adjacent layers were constructed with different rotation angles, which was in good agreement with the HAADF image (above column in Fig. 2). The corresponding FFT image (middle column of Fig. 2) also confirmed the angle of the HAADF image. The twisted angles of 0°, 6°, 12°, 18°, 24° and 30° existed in nanosheets from the HAADF and FFT images.

In order to quantify the angle of statistical distribution, all the measured HAADF images were divided into individual 50 nm × 50 nm regions, which were then counted (Fig. 2m–o and S14†). In Zr–BTB–MeOH, a total of 922 regions were collected, and the rotation angles were mainly 0° (77.01%). In Zr–BTB–EtOH, 0° dominated (83.45%) in 747 regions. In Zr–BTB–PrOH, 0° took up most of the 506 regions (85.61%). Other angles of 6°, 12°, 18°, 24° and 30° up to 11.60% were observed in Zr–BTB–MeOH. Meanwhile, a wide distribution of twisted angles was also found in Zr–BTB–EtOH and Zr–BTB–PrOH.

To explain the regulation effect of polar alcohol, the polarity interactions between alcohol and $Zr_6$ clusters were first evaluated. In the Zr–BTB nanosheets, the upper and lower six open sites of $Zr_6$ are only occupied with two formic acid molecules (Fig. S2–S4†), and the remaining four sites were coordinated by –OH or $–OH_2$, so the $Zr_6$ clusters were the only polar sites on the material. During the washing process, large amounts of alcoholic solvents were present, and the –OH of alcoholic solvents interacted with the $Zr_6$ cluster. To support this hypothesis, total energies and Bader charges of Zr–BTB–MeOH with different adsorption sites were calculated, respectively (Fig. 3). In the simulation, methanol was placed on the $Zr_6$–OH/$OH_2$ site and ligand site, respectively (Fig. 3a and b). The energy difference between two locations was 53.84 kJ $mol^{-1}$ (Fig. 3c). The energy of methanol adsorbed at the $Zr_6$ cluster was much lower than that of the ligand site in the Zr–BTB, which proved that methanol was indeed more easily adsorbed at the polar site. In addition, the Bader charges of methanol adsorbed at the $Zr_6$ cluster was 0.1475 ē, and that of the ligand site was only 0.0100 ē (Fig. 3c), indicating the contributions of van der Waals forces were enhanced at the $Zr_6$ cluster during methanol adsorption.

To explore the reason for untwisted stacking under the polar alcohol regulation, surface polarity and solvent effects were

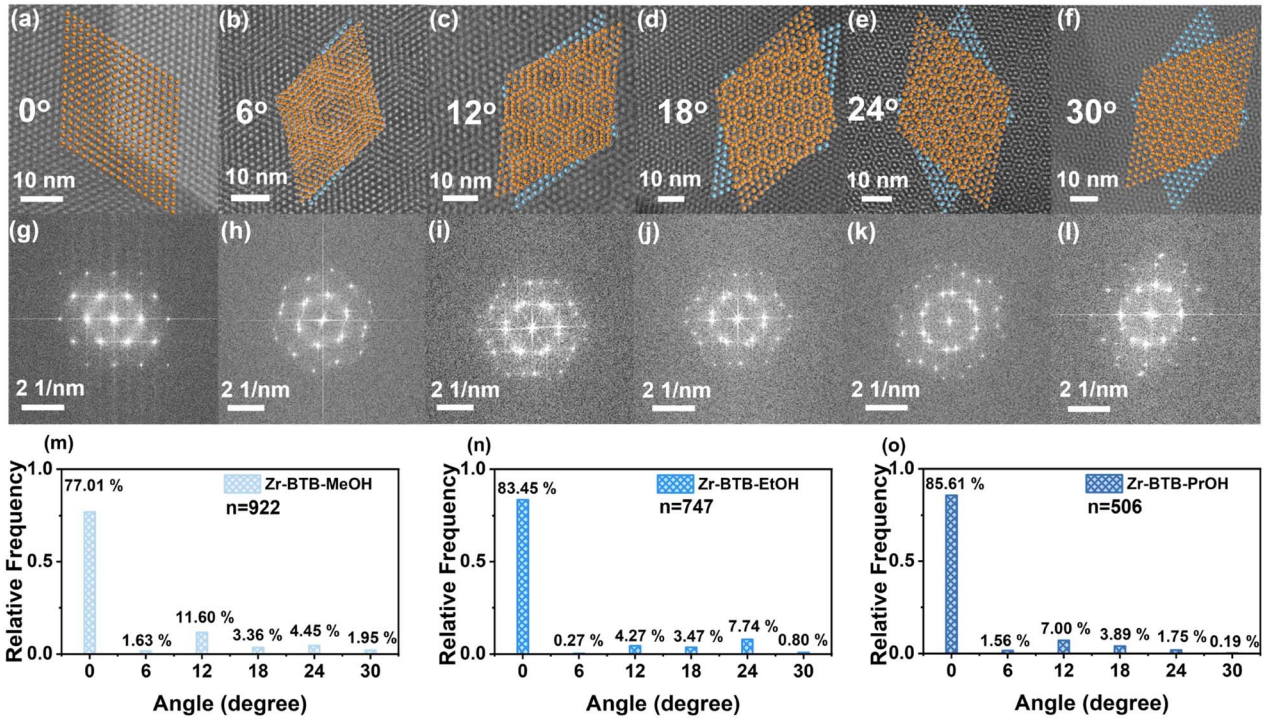


Fig. 2 Characterization and structural simulation of 2-D Zr–BTB–MeOH, Zr–BTB–EtOH, and Zr–BTB–PrOH nanosheet stacking. (a–f) HAADF images and the simulated double layers with the rotation of 0°, 6°, 12°, 18°, 24° and 30° from the left to the right. (g–l) The corresponding FFT images with the rotation of 0°, 6°, 12°, 18°, 24° and 30° from the left to the right. (m–o) The angular proportional distribution of 2-D Zr–BTB–MeOH, Zr–BTB–EtOH and Zr–BTB–PrOH nanosheets. The n represents the total counts. Each count represents the stacking angle in a unique 50 nm × 50 nm image.

analyzed. In the system, $Zr_6$ was weakly polar due to the $Zr_6$–OH/$OH_2$ of the nanosheets being exposed to the alkyl chain of the alcohol and the BTB ligands were non-polar, so BTB was compatible with BTB and $Zr_6$ matched well with $Zr_6$ between the adjacent layers. In addition, MOF nanosheets were weakly polar owing to the covered $Zr_6$–OH/$OH_2$ and non-polar BTB ligand, resulting in stronger non-polar interaction between the MOF nanosheets in polar solvents, so nanosheets easily generated regular stacking. Combining the two aspects, Zr–BTB nanosheets tended to form the pattern of untwisted stacking.

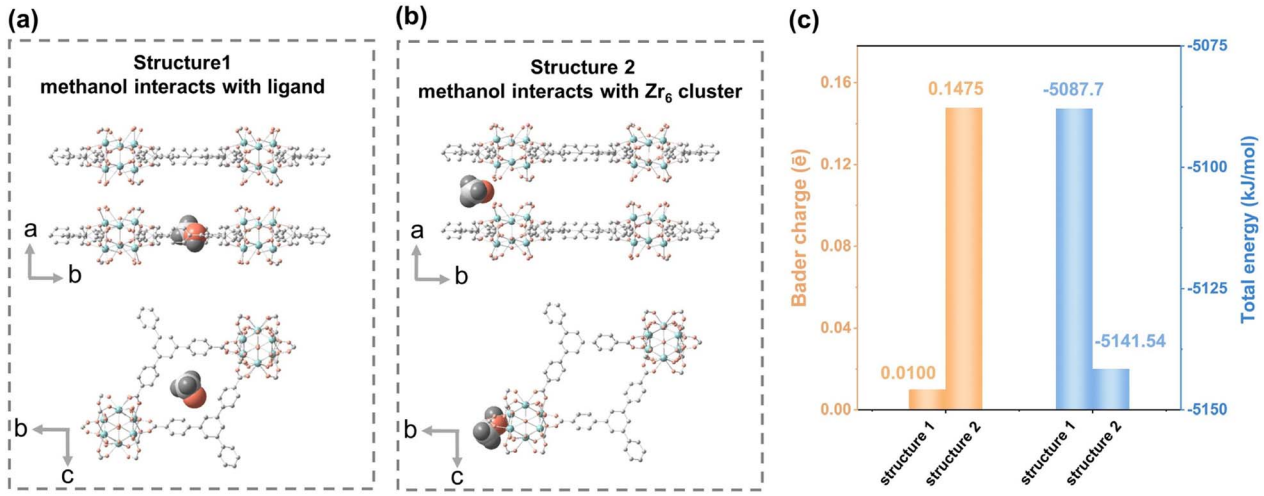


Fig. 3 Density functional theory (DFT) calculation for the methanol molecule at different locations in Zr–BTB nanosheets. (a) Structure 1 represents methanol interacting with the ligand of Zr–BTB. (b) Structure 2 represents methanol interacting with the $Zr_6$ cluster of Zr–BTB. The red ball stands for O, the green ball stands for Zr, and the gray ball stands for C. (c) The Bader charges between methanol and Zr–BTB and total energies of structure 1 and structure 2, respectively.

### 2-D Zr–BTB nanosheets for GC separation

The different pore environments of 2-D Zr–BTB nanosheets in twisted and untwisted stacking urged us to compare their separation abilities as GC stationary phases.[32] The uniform coating of nanosheets inside the columns is shown in the SEM images (Fig. S15†). The columns were then employed to separate substituted benzene isomers including dimethylbenzene, chlorotoluene, dichlorobenzene and ethyl toluene isomers. For all the isomers, all three Zr–BTB capillary columns exhibited good separation ability and showed special *para* selectivity (Fig. 4a–c and S16†). The resolution for different *meta* and *para* isomers was calculated for different columns, and the results showed that Zr–BTB–PrOH exhibited the highest resolution (Fig. 4d).

To understand the *para*-selectivity of the Zr–BTB columns, the van't Hoff curve was measured to calculate the enthalpy and entropy in the column (Fig. S17–S19, Tables S1 and S2†). The results showed that *p*-chlorotoluene, *p*-ethyl toluene, *p*-xylene and *p*-dichlorobenzene had the most negative $\Delta H$ among all the isomers. This indicated that the columns had the strongest interaction with the *para*-isomers, which fully explained the separation sequence of the column from a thermodynamic perspective.

Meanwhile, the suitable and uniform pore channels of 2-D nanosheets enhanced the kinetic diffusion of the analytes for distinguishing isomers because of the regular stacking.

In order to confirm the reproducibility and stability of 2 D Zr–BTB capillary GC columns, the performance of Zr–BTB–MeOH, Zr–BTB–EtOH and Zr–BTB–PrOH columns was tested (Fig. 4e, f, S20 and S21†). In five injections of chlorotoluene isomers, the same separation performance was obtained, indicating the good repeatability of the column. In addition, the column had a lifetime of at least 30 months without loss of column separation efficiency, showing the potential commercial value.

### Control experiments with 2-D Zr–TCA and Zr–TATB nanosheets

In order to verify the key role of the ligand in the stacking of nanosheets, we selected Zr–TCA and Zr–TATB as counterpart

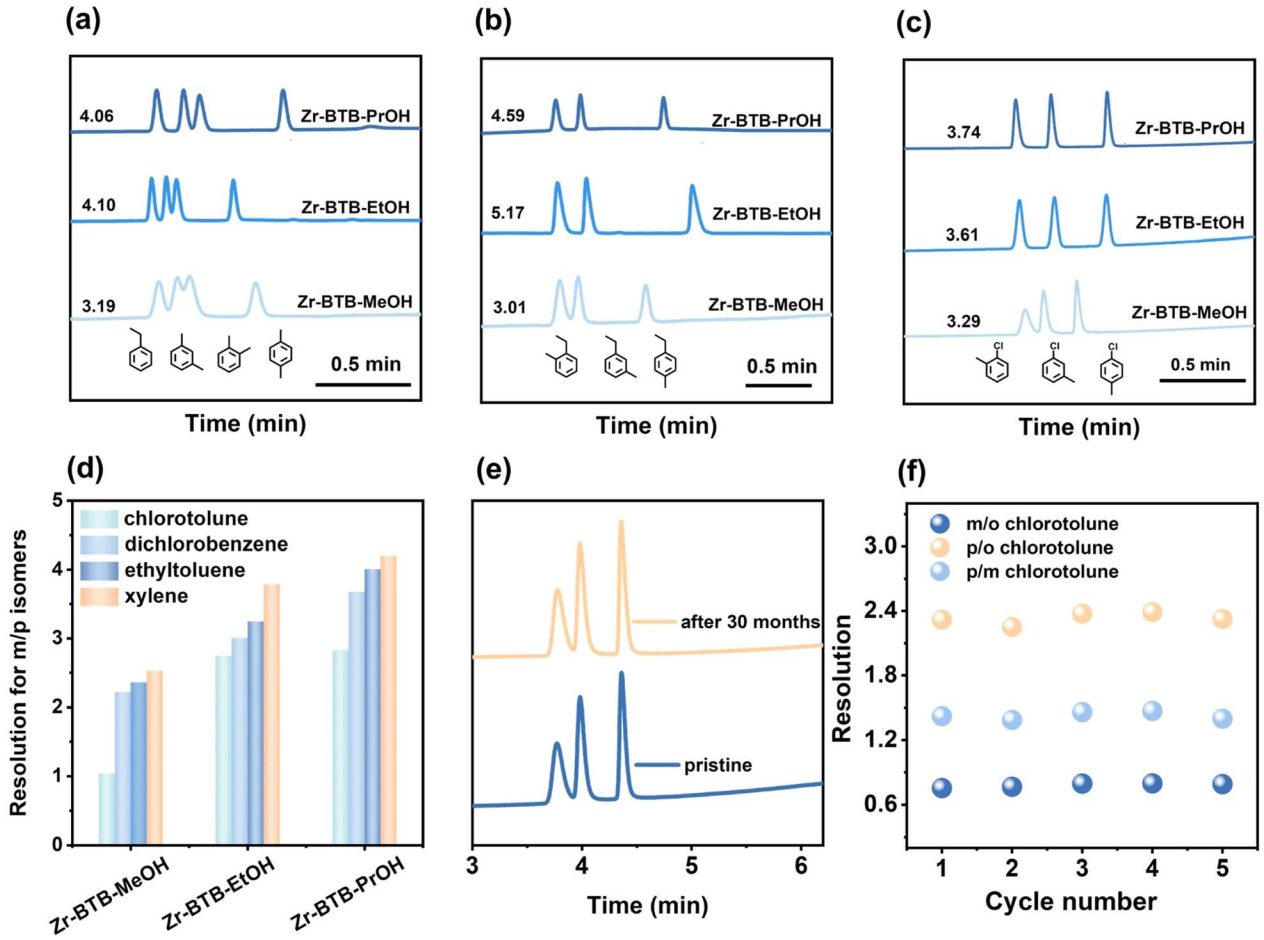


Fig. 4 Separation performance of 2-D Zr–BTB nanosheets. (a) Gas chromatograms using 2-D Zr–BTB nanosheet coated GC columns for the separation of xylene and ethyl benzene isomers, (b) ethyl toluene, and (c) chlorotoluene. (d) Resolution of 2-D Zr–BTB nanosheet coated GC columns. (e) The lifetime of the 2-D Zr–BTB–MeOH capillary column for separation of chlorotoluene isomers under the same experimental conditions within 30 months. (f) The thermal stability and repeatability of the 2-D Zr–BTB–MeOH capillary column for separation of chlorotoluene isomers 5 times continuously.

materials that were isomorphic to Zr–BTB nanosheets. The TCA ligand with an N atom and TATB with 1,3,5-triazine in the middle were the substituents for BTB with the benzene in the middle, so the polarities of TATB and TCA were slightly stronger than that of BTB. The Zr–TCA nanosheets were prepared by $H_3$TCA, and were then modulated by MeOH, EtOH and PrOH, accordingly. The Zr–TATB nanosheets were prepared by $H_3$TATB, and were modulated by EtOH. The washing steps of Zr–TCA and Zr–TATB followed an identical procedure, and detailed information can be found in the ESI.† PXRD measurements indicated the main peaks of the 2-D Zr–TCA and Zr–TATB were also in line with that of 2-D Zr–TCA and Zr–TATB simulation (Fig. 5a), which demonstrated the desired structures were successfully obtained after the washing steps. The TGA results of the 2-D Zr–TCA and Zr–TATB nanosheets indicated the excellent thermal stability (Fig. S22 and S23†).

All the water contact angle measurements were conducted at room temperature in ambient air (Fig. S24–S27†). The water contact angle exhibited a slight increase for the Zr–TCA–MeOH ($35.8 \pm 0.6°$), Zr–TCA–EtOH ($41.2 \pm 0.4°$), and Zr–TCA–PrOH ($47.1 \pm 0.3°$), which became more hydrophobic because of the increasing alkyl chains. The water contact angle of Zr–TATB was $44.4 \pm 0.6°$. Due to the presence of the polar hydroxyl group, the water contact angle of the nanosheets remained below 90°, reflecting their inherently highly hydrophilic properties. The HNMR indicated that $n$(MeOH/EtOH/PrOH) : $n$($Zr_6$) of Zr–TCA was 0.4, 2.0, and 2.4, and the $n$(EtOH) : $n$($Zr_6$) of Zr–TATB was 0.6, respectively (Fig. S28–S31†).

The high proportion of alcohol was due to the strong polar interaction between the nanosheets and –OH of alcoholic solvents. The morphology of the 2-D nanosheets was examined using SEM and TEM (Fig. S32 and S33†). In the SEM images of the 2-D Zr–TCA and Zr–TATB nanosheets, the multilayer nanosheets stacked, confirming 2-D lamellar structures. The thicknesses of Zr–TCA nanosheets were characterized by AFM measurements. They were $17.9 \pm 2.7$ nm, $31.5 \pm 1.1$ nm and $57.8 \pm 1.3$ nm for Zr–TCA–MeOH, Zr–TCA–EtOH, and Zr–TCA–PrOH, respectively (Fig. S34–S36†). The variation in nanosheet thickness was observed due to the different interaction influenced by the polarity of the solvent.

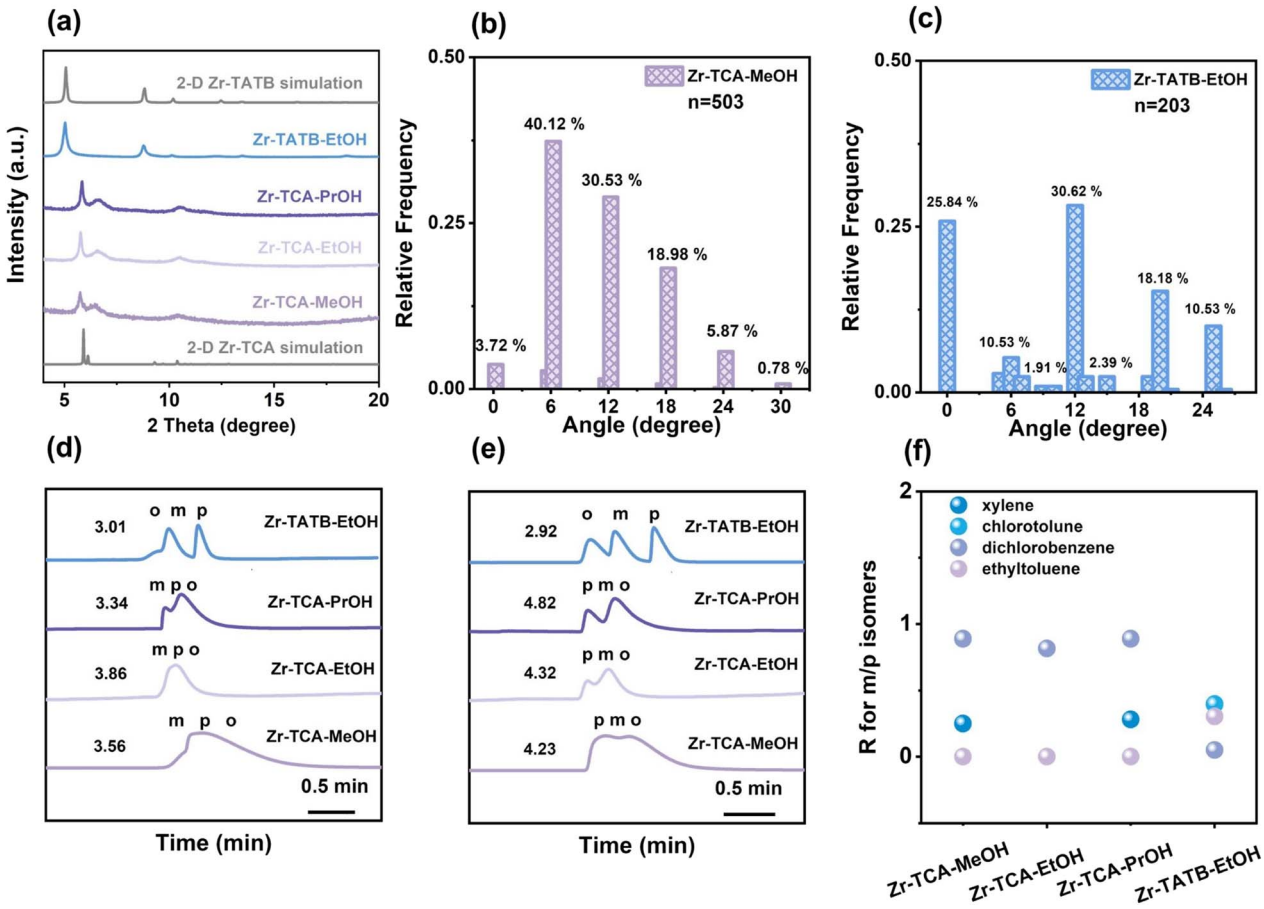


Fig. 5 The characterization and separation performance of 2-D Zr–TCA and Zr–TATB nanosheets. (a) PXRD patterns of Zr–TCA–MeOH, Zr–TCA–EtOH, Zr–TCA–PrOH, Zr–TATB–EtOH and simulated Zr–TCA and Zr–TATB. (b) The angular proportional distribution of 2-D Zr–TCA–MeOH from HAADF. (c) The angular proportional distribution of 2-D Zr–TATB–EtOH from HRTEM. The n represents the total counts. Each count represents the stacking angle in a unique 50 nm × 50 nm image. Gas chromatograms using 2-D Zr–TCA and Zr–TATB nanosheet coated GC columns for the separation of (d) ethyl toluene isomers and (e) chlorotoluene, respectively. (f) Resolution of different *p*-/*m*-isomers with 2-D Zr–TCA and Zr–TATB nanosheet coated GC columns.

To provide a more comprehensive explanation of stacking modes, HAADF images and FFT images of Zr–TCA–MeOH were measured. A total of 503 regions were counted (Fig. 5b). The twisted angles of Zr–TCA were 0°, 6°, 12°,18°, 24° and 30°, respectively. Among them, 6°, 12° and 18° played a leading role and three portions summed up to 89.63%. Consequently, it was observed that the Zr–TCA–MeOH nanosheets exhibited the twisted stacking modes, which was totally different from Zr–BTB. These nanosheets were mainly stable at the specific angle because the energy was lower than other angles, where the stacking mode by polar molecules was thermodynamically preferable.[22,29] Moreover, the corresponding FFT images also confirmed the angles observed in the HAADF images, providing further support for the accurate characterization of the nanosheet stacking structure. In the Zr–TCA–MeOH nanosheets, the $Zr_6$ site was not fully saturated, and the $Zr_6$–OH/$OH_2$ polar sites were present (Fig. S28†). At the same time, in the middle of the TCA ligand is a N atom, which showed the lone pair electron effect, while the center of BTB was a benzene ring, so the polarity of the TCA ligand was stronger than that of BTB.[33–35] Thus, the N sites of TCA, exposed $Zr_6$–OH/$OH_2$ and solvents are all polar, so the interactions are more complex, inducing the twisted nanosheets. In addition, the TCA ligands with triangular pyramidal structures easily generated wavy nanosheets, forming the twisted stacking nanosheets. In the Zr–TATB–EtOH nanosheets, the twisted angles of Zr–TATB–EtOH were 0°, 6°, 10°, 12°, 15°, 18°, and 24°, respectively from the HRTEM images and the corresponding FFT images, and a total of 203 regions were counted (Fig. 5c). In the TATB ligand, the electronegativity of C and N was different, so the polarity of TATB ligands was greater than that of BTB ligands.[36,37] Therefore, due to the existence of polar sites of $Zr_6$–OH/$OH_2$, the center of TATB and polar solvents in the system, the interaction was also complex, leading to the misplacing of two layers and the twisted stacked nanosheets.

Compared with Zr–BTB, the 2-D Zr–TCA and Zr–TATB nanosheets as GC stationary phases can provide different twisted and polar pores to show their separation abilities. Their successful coating onto the columns was verified from the SEM pictures (Fig. S37†) and these columns separated the same substituted benzene isomers. For all of the isomer pairs, 2-D Zr–TCA and Zr–TATB capillary columns exhibited relatively poor separation ability compared with Zr–BTB (Fig. 5d, e, S38 and S39†). The resolution of the four columns for *meta* and *para* isomers was all lower than 1 (Fig. 5f). In 2-D Zr–TCA capillary columns, the elution order of ethyl toluene isomers followed the boiling point sequence, while all the other isomers followed the *para*-selectivity. In 2-D Zr–TATB capillary columns, the other isomers showed *para*-selectivity, while the dichlorobenzene isomers followed a boiling point sequence (Fig. 5d, e and S39†). The phenomena may arise from the twisted stacking of Zr–TCA and Zr–TATB with a wide distribution of apertures.

## Conclusions

In summary, we used a series of alcohol guest molecules to modulate Zr–BTB nanosheets in untwisted stacking. MeOH, EtOH and PrOH modulated an untwisted stacking rate of 77.01%, 83.45%, and 85.61%, respectively. The resulting untwisted Zr–BTB nanosheets demonstrated excellent separation efficiency, outstanding positional selectivity, and remarkable column stability and reusability for different substituted benzene isomers. In contrast, the control experiments with similar 2-D Zr–TCA and Zr–TATB nanosheets modulated by alcohol guests resulted in twisted stacking and exhibited inferior separation performance. This provided strong host–guest interactions during the modulation of 2-D MOF nanosheet stacking, offering opportunities for designing novel porous Moiré materials with potential applications.

## Data availability

All relevant experimental and computational data and characterization details are provided in the ESI.†

## Author contributions

Z.-Y. G. conceived the idea and supervised the research. Y. C. and W.-Q. T. performed the synthesis, GC and characterization experiments and analyzed the data. L.-T. G., J.-P. Z., and S.-S. M. assisted with the GC experiments. Z.-Y. G., M. X. and C. Y. discussed the experimental data and wrote the paper.

## Conflicts of interest

There are no conflicts to declare.

## Acknowledgements

This work is supported by the National Natural Science Foundation of China (22174067, 22204078 and 22374077), the Natural Science Foundation of Jiangsu Province of China (BK20220370), Jiangsu Provincial Department of Education (22KJB150009), State Key Laboratory of Analytical Chemistry for Life Science (SKLACLS2218), the Priority Academic Program Development of Jiangsu Higher Education Institutions, and Postgraduate Research & Practice Innovation Program of Jiangsu Province (KYCX23_1686). This work is carried out with the support of Shanghai Synchrotron Radiation Facility Beamline BL17B1 (proposal 2021-NFPS-PT-006657).

## Notes and references

1 P. Ball, *Nat. Mater.*, 2022, **21**, 838.
2 M. Liu, L. Wang and G. Yu, *Adv. Sci.*, 2022, **9**, 2103170.
3 M. Brzhezinskaya, O. Kononenko, V. Matveev, A. Zotov, I. I. Khodos, V. Levashov, V. Volkov, S. I. Bozhko, S. V. Chekmazov and D. Roshchupkin, *ACS Nano*, 2021, **15**, 12358–12366.
4 C. Liu, Z. Li, R. Qiao, Q. Wang, Z. Zhang, F. Liu, Z. Zhou, N. Shang, H. Fang, M. Wang, Z. Liu, Z. Feng, Y. Cheng, H. Wu, D. Gong, S. Liu, Z. Zhang, D. Zou, Y. Fu, J. He, H. Hong, M. Wu, P. Gao, P.-H. Tan, X. Wang, D. Yu,

E. Wang, Z.-J. Wang and K. Liu, *Nat. Mater.*, 2022, **21**, 1263–1268.
5 D. Wong, K. P. Nuckolls, M. Oh, B. Lian, Y. Xie, S. Jeon, K. Watanabe, T. Taniguchi, B. A. Bernevig and A. Yazdani, *Nature*, 2020, **582**, 198–202.
6 K. F. Mak and J. Shan, *Nat. Nanotechnol.*, 2022, **17**, 686–695.
7 M. Liao, Z. Wei, L. Du, Q. Wang, J. Tang, H. Yu, F. Wu, J. Zhao, X. Xu, B. Han, K. Liu, P. Gao, T. Polcar, Z. Sun, D. Shi, R. Yang and G. Zhang, *Nat. Commun.*, 2020, **11**, 2153.
8 Y. Cao, V. Fatemi, S. Fang, K. Watanabe, T. Taniguchi, E. Kaxiras and P. Jarillo-Herrero, *Nature*, 2018, **556**, 43–50.
9 M.-L. Lin, Q.-H. Tan, J.-B. Wu, X.-S. Chen, J.-H. Wang, Y.-H. Pan, X. Zhang, X. Cong, J. Zhang, W. Ji, P.-A. Hu, K.-H. Liu and P.-H. Tan, *ACS Nano*, 2018, **12**, 8770–8780.
10 L. Xie, L. Wang, W. Zhao, S. Liu, W. Huang and Q. Zhao, *Nat. Commun.*, 2021, **12**, 5070.
11 X. Hu, Z. Wang, Y. Su, P. Chen, Y. Jiang, C. Zhang and C. Wang, *Chem. Mater.*, 2021, **33**, 1618–1624.
12 R.-B. Lin, S. Xiang, W. Zhou and B. Chen, *Chem*, 2020, **6**, 337–363.
13 J. Lv, W. Li, J. Li, Z. Zhu, A. Dong, H. Lv, P. Li and B. Wang, *Angew. Chem., Int. Ed.*, 2023, **62**, e202217958.
14 L. Lei, F. Chen, Y. Wu, J. Shen, X.-J. Wu, S. Wu and S. Yuan, *Sci. China: Chem.*, 2022, **65**, 2205–2213.
15 J. Dong, X. Li, K. Zhang, Y. D. Yuan, Y. Wang, L. Zhai, G. Liu, D. Yuan, J. Jiang and D. Zhao, *J. Am. Chem. Soc.*, 2018, **140**, 4035–4046.
16 Y. Liu, L. Liu, X. Chen, Y. Liu, Y. Han and Y. Cui, *J. Am. Chem. Soc.*, 2021, **143**, 3509–3518.
17 A. Cadiau, L. S. Xie, N. Kolobov, A. Shkurenko, M. Qureshi, M. R. Tchalala, S. S. Park, A. Bavykina, M. Eddaoudi, M. Dincă, C. H. Hendon and J. Gascon, *Chem. Mater.*, 2020, **32**, 97–104.
18 H. Zeng, X.-J. Xie, M. Xie, Y.-L. Huang, D. Luo, T. Wang, Y. Zhao, W. Lu and D. Li, *J. Am. Chem. Soc.*, 2019, **141**, 20390–20396.
19 M. Xu, P. Cai, S. Meng, Y. Yang, D. Zheng, Q. Zhang, L. Gu, H. Zhou and Z. Gu, *Angew. Chem., Int. Ed.*, 2022, **61**, e202207786.
20 H. Hao, Y. Zhao, D. Chen, J. Yu, K. Tan, S. Ma, Y. Chabal, Z. Zhang, J. Dou, Z. Xiao, G. Day, H. Zhou and T. Lu, *Angew. Chem., Int. Ed.*, 2018, **57**, 16067–16071.
21 Y. Wang, L. Feng, J. Pang, J. Li, N. Huang, G. S. Day, L. Cheng, H. F. Drake, Y. Wang, C. Lollar, J. Qin, Z. Gu, T. Lu, S. Yuan and H. Zhou, *Adv. Sci.*, 2019, **6**, 1802059.
22 X. Liu, A. Wang, C. Wang, J. Li, Z. Zhang, A. M. Al-Enizi, A. Nafady, F. Shui, Z. You, B. Li, Y. Wen and S. Ma, *Nat. Commun.*, 2023, **14**, 7022.
23 X. Li, D. Sensharma, V. I. Nikolayenko, S. Darwish, A. A. Bezrukov, N. Kumar, W. Liu, X.-J. Kong, Z. Zhang and M. J. Zaworotko, *Chem. Mater.*, 2023, **35**, 783–791.
24 H. Zhou, L. Zhang, G. Wang, Y. Zhang, X. Wang, M. Li, F. Fan, Y. Li, T. Wang, X. Zhang and Y. Fu, *ACS Appl. Mater. Interfaces*, 2021, **13**, 39755–39762.
25 T. Si, X. Lu, H. Zhang, S. Wang, X. Liang and Y. Guo, *Chin. Chem. Lett.*, 2022, **33**, 3869–3872.
26 B. Tang, W. Wang, H. Hou, Y. Liu, Z. Liu, L. Geng, L. Sun and A. Luo, *Chin. Chem. Lett.*, 2022, **33**, 898–902.
27 Z.-R. Tao, J.-X. Wu, Y.-J. Zhao, M. Xu, W.-Q. Tang, Q.-H. Zhang, L. Gu, D.-H. Liu and Z.-Y. Gu, *Nat. Commun.*, 2019, **10**, 2911.
28 W. Tang, Y. Zhao, M. Xu, J. Xu, S. Meng, Y. Yin, Q. Zhang, L. Gu, D. Liu and Z. Gu, *Angew. Chem., Int. Ed.*, 2021, **60**, 6920–6925.
29 W.-Q. Tang, X. Yi, H. Guan, X.-W. Wang, Y.-W. Gu, Y.-J. Zhao, J. Fu, W. Li, Y. Cheng, S.-S. Meng, M. Xu, Q.-H. Zhang, L. Gu, X. Kong, D.-H. Liu, W. Wang and Z.-Y. Gu, *J. Am. Chem. Soc.*, 2023, **145**, 26580–26591.
30 C. J. Shock, M. J. Stevens, A. L. Frischknecht and I. Nakamura, *J. Chem. Phys.*, 2023, **159**, 134507.
31 L. Feng, Y. Qiu, Q.-H. Guo, Z. Chen, J. S. W. Seale, K. He, H. Wu, Y. Feng, O. K. Farha, R. D. Astumian and J. F. Stoddart, *Science*, 2021, **374**, 1215–1221.
32 H.-L. Qian, C.-X. Yang and X.-P. Yan, *Nat. Commun.*, 2016, **7**, 12104.
33 J. Han, Y. Yang, Y. Gong, X. Tang, Y. Tian and B. Li, *Nat. Commun.*, 2023, **14**, 5148.
34 Y.-Y. Ji, Z.-L. Wang, F.-N. Pei, J.-J. Shi, J.-J. Li, H. Gunosewoyo, F. Yang, J. Tang, X. Xie and L.-F. Yu, *MedChemComm*, 2019, **10**, 2131–2139.
35 B. Cosgrove, K. Down, S. Bertrand, N. C. O. Tomkinson and M. D. Barker, *Bioorg. Med. Chem. Lett.*, 2021, **33**, 127752.
36 Y. Shen, C. Chen, Z. Zou, Z. Hu, Z. Fu, W. Li, S. Pan, Y. Zhang, H. Zhang, Z. Yu, H. Zhao and G. Wang, *J. Catal.*, 2023, **421**, 65–76.
37 Y. Huang, D. Li, Z. Fang, R. Chen, B. Luo and W. Shi, *Appl. Catal., B*, 2019, **254**, 128–134.